

Supplementary Information

Experimental Validation of High Thermoelectric Performance in $RECuZnP_2$ Predicted by High-Throughput DFT Calculations

Jan-Hendrik Pöhls, Sevan Chanakian, Junsoo Park, Alex M. Ganose, Alexander Dunn, Nick Friesen, Amit Bhattacharya, Brea Hogan, Sabah Bux, Anubhav Jain, Arthur Mar, and Alexandra Zevalkink**

1. Experimental Methods

1.1. Sample Preparation

$RECuZnP_2$ ($RE = Pr, Nd, Er$) compounds were prepared by solid state reactions. Stoichiometric amounts of freshly filed RE pieces (99.9%, Hefa), Cu powder (99.5%, Alfa-Aesar), Zn shot (99.99%, Sigma-Aldrich), and red P powder (99.99%, Sigma-Aldrich) were combined, with a 10% excess of P added to compensate for volatilization losses, in a total mass of 0.3 g. The mixture was pressed into a pellet and placed in a carbon-coated fused-silica tube, which was evacuated (0.001 mbar) and sealed. The carbon coating serves to minimize attack on the tube, and to remove oxygen from Cu and Zn metal. The samples were heated to 500 °C over 24 h, held there for 48 h, heated to 900 °C, held there for 7 d, and then cooled down to room temperature over 48 h. The products were reground and repressed, and the heat treatment was repeated. This procedure led to nearly phase pure samples.

The samples were placed in a stainless steel SPEX mill vial equipped with two half-inch stainless steel ball bearings. They were ball-milled for 10 min and turned into fine-grained powders in preparation for spark plasma sintering (SPS), for which the particle size is critical to ensure densification. The powders were placed into a graphite die and sintered in a Dr. Sinter SPS-211LX apparatus at 800 °C for 5 min under a pressure of 45 MPa, followed by radiative cooling to room temperature under a pressure of 5 MPa. The Er-containing sample was reprocessed because the initial pressing parameters and particle size were insufficient for proper densification. The sintered samples had a diameter of 10 mm and thickness of 2 mm. They were polished to obtain flat, parallel surfaces.

1.2. X-ray Diffraction Analysis

Powder X-ray diffraction (XRD) patterns of the ground samples were collected on an Inel diffractometer equipped with a curved position-sensitive detector (CPS120) and a Cu $K\alpha_1$ radiation source and a Rigaku Smartlab diffractometer with Cu $K\alpha$ radiation. The samples were analyzed before and after consolidation to confirm that no structural changes occurred. Le Bail fittings were applied to the powder XRD patterns (**Figure S1**). The refined cell parameters agree well with those previously reported (**Table S1**).^[1]

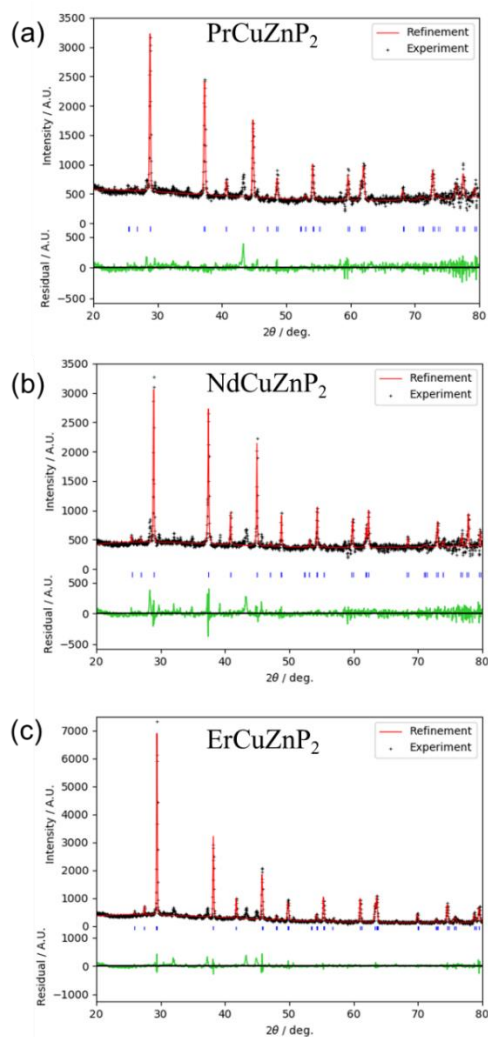
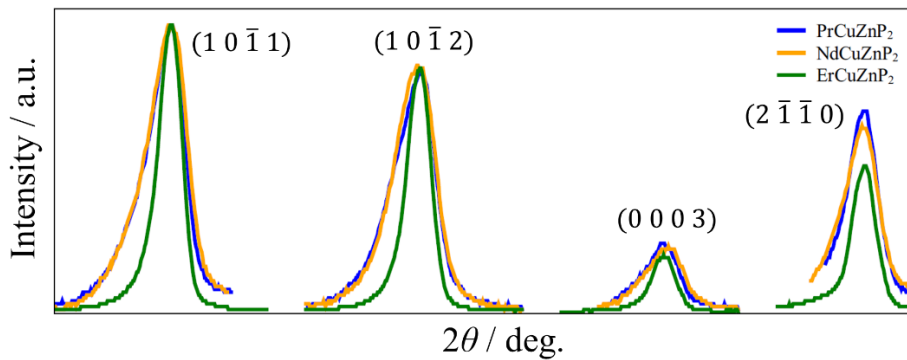


Figure S1. Le Bail fittings of powder X-ray diffraction patterns for (a) PrCuZnP_2 , (b) NdCuZnP_2 , and (c) ErCuZnP_2 . Blue tic marks show peak positions and green curve is the difference plot. Minor amounts of $\text{RECu}_5/\text{REZn}_5$ (in PrCuZnP_2 and NdCuZnP_2) and Er_2O_3 (in ErCuZnP_2) were observed.

Table S1. Refined lattice parameters of PrCuZnP₂, NdCuZnP₂, and ErCuZnP₂.

Compound	$a / \text{\AA}$	$c / \text{\AA}$	$V / \text{\AA}^3$	Ref.
PrCuZnP ₂	4.047(1)	6.661(1)	94.5(1)	[1]
PrCuZnP ₂	4.047(9)	6.654(1)	94.4(4)	This work
NdCuZnP ₂	4.024(1)	6.615(2)	92.8(1)	[1]
NdCuZnP ₂	4.035(1)	6.621(7)	93.4(1)	This work
ErCuZnP ₂	3.958(1)	6.479(1)	87.9(1)	[1]
ErCuZnP ₂	3.958(9)	6.484(8)	88.0(5)	This work

Close inspection reveals that the diffraction peaks are consistently narrower in ErCuZnP₂ than in PrCuZnP₂ or NdCuZnP₂ (**Figure S2**). Qualitatively, this observation suggests that the grain sizes are larger in the Er-containing sample.

**Figure S2.** Comparison of breadths of major diffraction peaks suggests that the ErCuZnP₂ sample has larger grain sizes.

The RECuZnP₂ (RE = Pr, Nd, Er) compounds crystallize in the trigonal CaAl₂Si₂-type structure. The structure consists of anionic [MP₂]³⁻ layers (M = Cu, Zn) stacked along the *c*-direction and separated by RE³⁺ cations (**Figure S3**).^[1] Alternatively, the structure can be

described as a stacking of nets of P atoms in an hcp sequence, with half the octahedral sites occupied by *RE* atoms, and half the tetrahedral sites by *M* atoms. The Cu and Zn atoms are disordered over the *M* site located at $2d$ ($1/3, 2/3, \sim 0.63$). The relatively open space between the layers and the disorder of *M* atoms are structural features that may be conducive to low thermal conductivity. Other CaAl_2Si_2 -type compounds have been demonstrated to show high thermoelectric efficiency, such as EuZn_2Sb_2 ,^[2] EuCd_2Sb_2 ,^[3] and YbZn_2Sb_2 .^[4] These layered compounds exhibit enhanced electrical conductivity within the planes while showing only a slight increase in thermal conductivity.

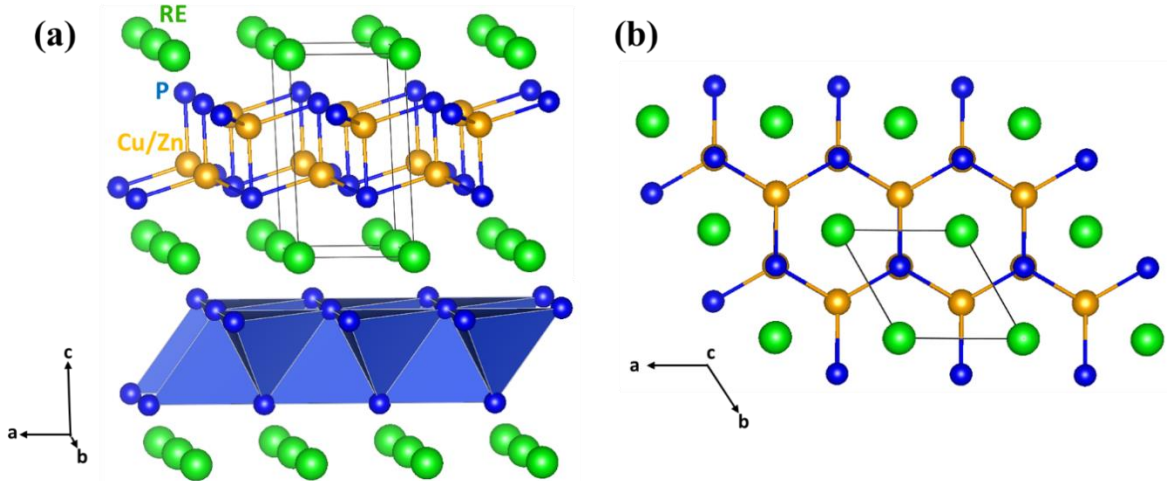


Figure S3. Crystal structure of RECuZnP_2 viewed (a) perpendicular to and (b) along the *c*-direction. The Cu and Zn atoms are disordered over tetrahedral sites.

1.3. Physical Property Measurements

Elastic properties were determined via resonant ultrasound spectroscopy using an ACE-RUS008 system with a TS 001 stage.^[5] The samples were measured at a frequency sweep of 50 to 400 kHz and a transducer output amplitude of 50 mV. Electrical resistivities and Hall coefficients were measured on a custom-built instrument. Tungsten electrodes were mechanically mounted onto samples in a four-point probe geometry. For Hall measurements, an external magnetic field of ± 0.8 T was applied. Seebeck coefficients were measured on a custom-built instrument with

axially applied thermocouples and thermal gradient. A temperature gradient of ± 5 K was applied, and the Seebeck coefficient was extracted from a linear fit of the voltage vs temperature gradient curve. Thermal diffusivities α were measured on a Netzsch LFA-457 laser flash apparatus. The pellets were coated in graphite to enhance blackbody radiation. The thermal conductivity was calculated from the relationship $\kappa = \alpha \cdot C_p \cdot d$, where d is the mass density and C_p is the heat capacity at constant pressure. The heat capacity was approximated, following the Neumann-Kopp law, as the weighted sum of the molar heat capacities of the component elements. Uncertainties in the thermal conductivity were evaluated by taking three consecutive measurements of the thermal diffusivity, and 5% from the density and heat capacity at constant pressure. Uncertainties in the thermoelectric figure of merit are set to 15%.

2. Computational Methods

2.1 High-fidelity density functional theory calculations

Density functional theory (DFT) calculations were performed using the Vienna Ab Initio Simulation Package (VASP)^[6] employing a plane-wave basis set and projector-augmented wave (PAW) pseudopotentials.^[7] Given the computational expense of compressive-sensing lattice dynamics (CSLD) calculations,^[8] the disordered crystal structures of $RECuZnP_2$, determined experimentally from X-ray diffraction, were modeled as ordered structures containing 5 atoms per unit cell. Geometry relaxations and all supercell calculations were performed using the Perdew-Burke-Ernzerhof generalized-gradient approximation (PBE-GGA)^[9] exchange correlation functional. For geometry optimizations, the cut-off energy was set to 500 eV and a $12 \times 12 \times 6$ k -point mesh was used for convergence. To evaluate the influence of Cu/Zn disorder, two disordered configurations in a 2x2x2 supercell were computed: one a quasi-random structure – maximizing

disorder – and the other a “super-ordered” structure. The latter is lower in energy by (~ 13 meV atom⁻¹ for ErZnCuP₂) and identical in energy to the perfectly ordered, 5-atom primitive cell.

Electronic properties, including band structures, density of states, and dielectric constants, were calculated using the Heyd-Scuseria-Ernzerhof (HSE06) hybrid functional.^[10] A k -point mesh of $6 \times 6 \times 3$ was sufficient to provide convergence for band gaps and dielectric constants.

Dielectric constants were calculated using the Perturbation Expression After Discretization (PEAD) approach of Nunes and Gonze,^[11] and Souza et al.^[12] Due to self-interaction errors present in density functional theory, partially filled f states can often lead to large errors for rare earth elements. For this reason, we use the Pr_3, Nd_3, and Er_3 VASP pseudopotentials in which 2, 3, 11 f-electrons are treated as core states, respectively.

The electronic band structures reveal small band gaps of 0.52 eV for NdCuZnP₂, 0.54 eV for PrCuZnP₂, and 0.73 eV for ErCuZnP₂ (**Figure S4**). The valence band maximum is located at Γ and the conduction band minimum is located at L.

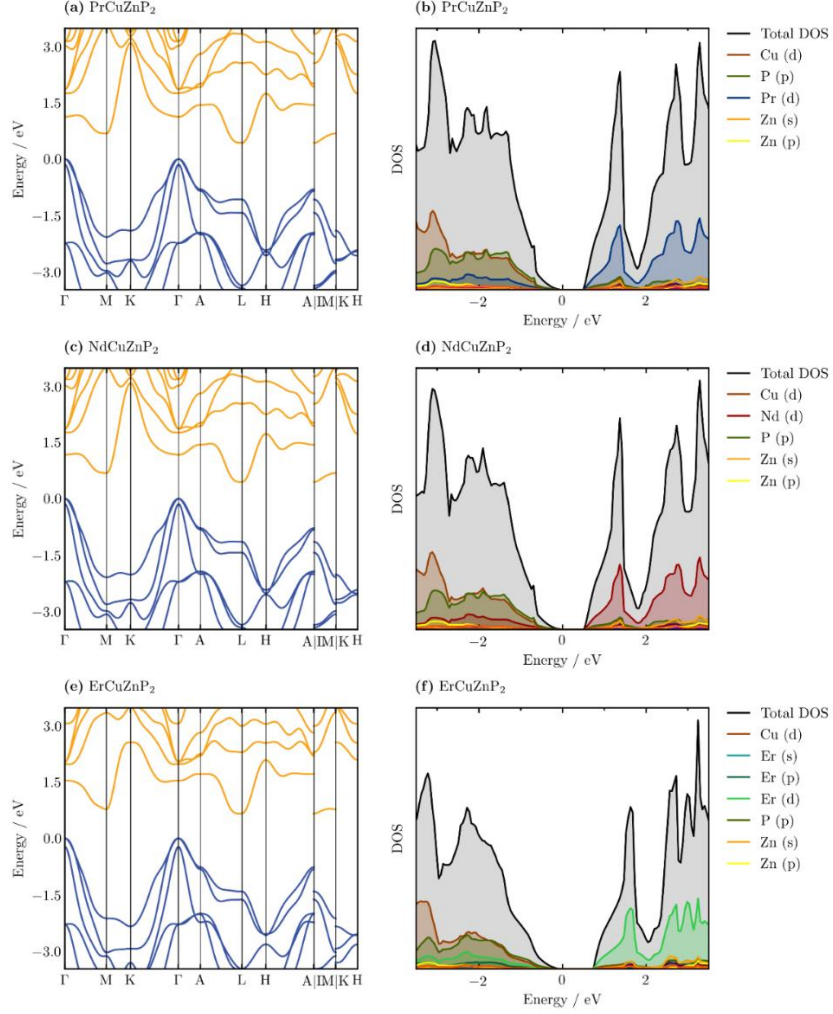


Figure S4. HSE06 electronic band structures and density of states (DOS) for (a,b) PrCuZnP₂, (c,d) NdCuZnP₂, and (e,f) ErCuZnP₂. No significant differences were observed among the three electronic band structures.

Harmonic and anharmonic interatomic force constants were calculated using CLSD.^[8]

For fitting, twenty training $4 \times 4 \times 3$ supercells were set up containing 240 atoms randomly displaced by up to 0.05 \AA . An energy cut-off of 500 eV and k -point mesh of $3 \times 3 \times 2$ were used. Pair and triplet clusters were selected within cut-off diameters of 8 and 4.5 \AA , and 10% of sample clusters were held out for cross-validation whose error was low ($\sim 4\%$).

Lattice thermal conductivity was calculated using first-order perturbation theory for three phonon scattering, as implemented in ShengBTE^[13] using the force constants obtained from

CSLD. Previous studies have established that these methods are robust for accurately predicting lattice thermal conductivity. A $24 \times 24 \times 20$ \mathbf{q} -point mesh led to well-converged results. The thermal conductivity was found to be highest parallel to the layers in the crystal structure and lowest perpendicular to the layers, consistent with the relative strengths of bonding interactions in the structure. ErCuZnP_2 has a slightly higher thermal conductivity than NdCuZnP_2 because of its shorter bonds and stronger interatomic forces. To compare with the experimental thermal conductivities, which were measured on polycrystalline samples of RECuZnP_2 , the harmonic average of the calculated thermal conductivities along the three Cartesian directions was taken as $\kappa_{poly} = 3/(2 \cdot \kappa_{x,y}^{-1} + \kappa_z^{-1})$, where $\kappa_{x,y}$ is the in-plane and κ_z is the out-of-plane thermal conductivity. This value represents the lower Wiener bound for composite materials.

Electronic transport properties (electrical resistivity, electronic contribution to the thermal conductivity, Seebeck coefficient, and hole mobility) were calculated within the AMSET formalism (<https://hackingmaterials.lbl.gov/amset/>), which explicitly includes band and \mathbf{k} -point dependent scattering rates. In this approach, transport properties were determined assuming the momentum relaxation time approximation to the Boltzmann transport equation, with band structures and wavefunctions obtained using the HSE06 functional. As has been described in detail elsewhere,^[14] scattering rates were calculated from materials parameters obtained from first principles (**Table S2**). In this work, the scattering mechanisms considered were ionized impurity scattering, acoustic deformation potential scattering, and polar optical phonon scattering. The scattering matrix elements $g(\mathbf{k}, \mathbf{q})$ represent the probability of scattering from electronic state $|\mathbf{k}\rangle$ to state $|\mathbf{k} + \mathbf{q}\rangle$, according to:

$$g^{\text{imp}}(\mathbf{k}, \mathbf{q}) = \left[\frac{e^2 n_{\text{ii}}}{\epsilon_s^2} \right]^{\frac{1}{2}} \frac{\langle \psi_{\mathbf{k}+\mathbf{q}} | \psi_{\mathbf{k}} \rangle}{|\mathbf{q}|^2 + \beta^2} \quad (1)$$

$$g^{\text{adp}}(\mathbf{k}, \mathbf{q}) = \left[\frac{k_B T \varepsilon_d^2}{B} \right]^{\frac{1}{2}} \langle \psi_{\mathbf{k}+\mathbf{q}} | \psi_{\mathbf{k}} \rangle \quad (2)$$

$$g^{\text{pop}}(\mathbf{k}, \mathbf{q}) = \left[\frac{\hbar \omega_{\text{po}}}{2} \left(\frac{1}{\varepsilon_{\infty}} - \frac{1}{\varepsilon_s} \right) \right]^{\frac{1}{2}} \frac{\langle \psi_{\mathbf{k}+\mathbf{q}} | \psi_{\mathbf{k}} \rangle}{|q|} \quad (3)$$

where T is temperature, e is the electron charge, \hbar is the reduced Planck constant, k_B is the Boltzmann constant, n_{ii} is the concentration of ionized impurities, β is the inverse screening length calculated from the density of states, $\psi_{\mathbf{k}}$ is the wavefunction of state $|\mathbf{k}\rangle$, ε_s is the static dielectric constant, ε_{∞} is the high-frequency dielectric constant, ε_d is the volume-deformation potential at the valence band maximum, B is the bulk modulus, and ω_{po} is an effective optical phonon frequency. These expressions require only material-dependent parameters which can be computed relatively quickly from first principles (**Table S1**).^[14] Because it is not feasible to determine the exact ionized impurity concentration, the concentration was set equal to the number of free carriers (electrons + holes). The exact value should maximally differ to n_{ii} by a factor of 2-3 (i.e., if charge compensation is significant). Previous calculations indicated that this approach could accurately reproduce the mobility of Si and GaAs as function of carrier concentration.^[15]

Owing to convergence problems, the static and high-frequency dielectric constant and the polar optical phonon frequency could not be obtained for ErCuZnP₂. However, given that the electrical and vibrational properties of ErCuZnP₂ and NdCuZnP₂ are exceedingly similar, the values obtained for NdCuZnP₂ were used in both cases.

Table S2. Materials parameters for PrCuZnP₂, NdCuZnP₂, and ErCuZnP₂ used in AMSET calculations of electronic transport properties. ϵ_s and ϵ_∞ are the static and high-frequency dielectric constants, E_d^{VBM} is the volume deformation potential at the valence band maximum (VBM), B is the bulk modulus, and ω_{po} is the effective polar optical phonon frequency.

Compound	ϵ_s	ϵ_∞	$E_d^{\text{VBM}} / \text{eV}$	B / GPa	$\omega_{\text{po}} / \text{THz}$
PrCuZnP ₂	26.29	14.54	1.39	86.88	6.46
NdCuZnP ₂	26.33	14.23	1.40	88.00	6.49
ErCuZnP ₂	26.33	14.23	1.69	94.03	6.49
CaZn ₂ P ₂	16.53	8.79	1.75	61.12	7.26

This method has the benefit to compute the mobilities for the individual scattering mechanism as a function of temperature (**Figure S5**). All three compounds exhibit mobilities limited by polar optical phonons. In fact, acoustic deformation potential is more than two orders of magnitude higher than the overall mobility suggesting that acoustic deformation potential is not a major contributor to scattering in these compounds.

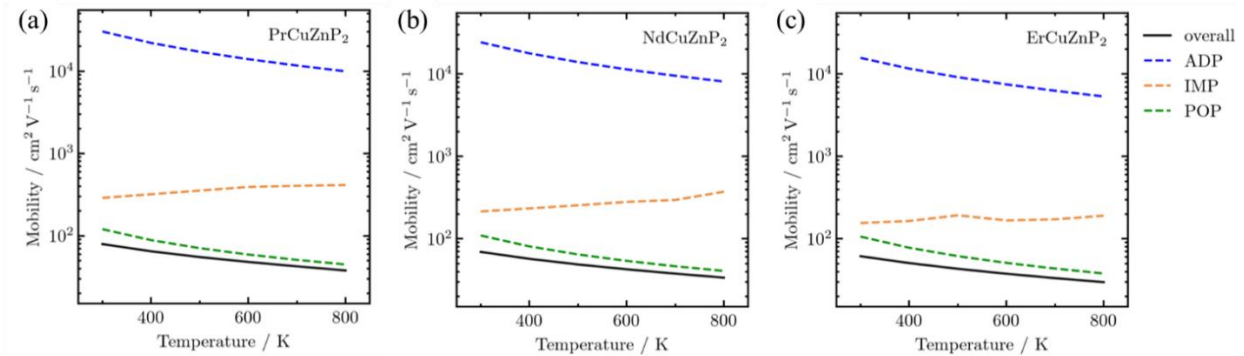


Figure S5: Theoretical mobilities of (a) PrCuZnP₂, (b) NdCuZnP₂, and (c) ErCuZnP₂ as a function of temperature separated in acoustic deformation potential (ADP), ionized impurity (IMP), and polar optical phonon (POP) scattering. Mobilities decrease with atomic number of RE and temperature.

The same trend of the scattering mechanisms was observed for the simpler (i.e. does not contain f-electrons and disorder on the metal site) compound CaZn₂P₂ (**Figure S6**). The total mobility in

CaZn_2P_2 is only half of that for RECuZnP_2 due to a decrease in dielectric constants and increase in the effective polar optical phonon frequency (**Table S2**).

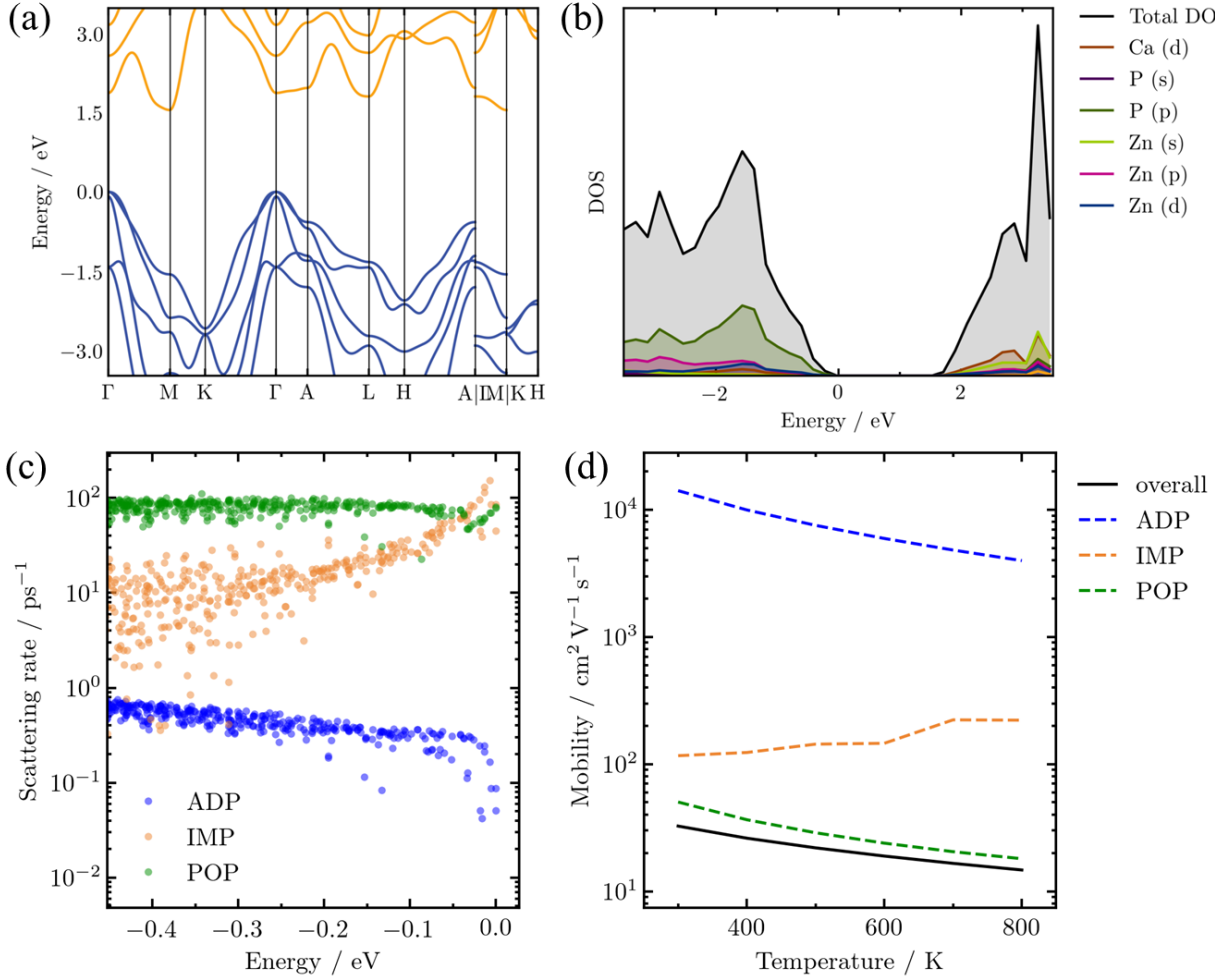


Figure S6: (a) HSE06 electronic band structure, (b) DOS, (c) scattering rate, and (d) mobility of CaZn_2P_2 . Smaller separation of valence bands at Γ leads to higher conductivity effective mass. Like RECuZnP_2 , hole mobility of CaZn_2P_2 is limited by polar-optical phonon (POP) and ionized impurity (IMP) scattering. Acoustic deformation phonon (ADP) scattering does not significantly affect the mobility.

2.2. Computational Screening of Disordered Materials

Disordered crystalline materials present great opportunity for thermoelectric applications, as many have not been examined for thermoelectric merit. To identify promising yet unexplored candidates for thermoelectric devices, we undertook a high-throughput, machine learning (ML)-guided

screening of 20,211 disordered (partial occupancy) materials from the 2017 edition of the Inorganic Crystal Structure Database (ICSD).^[16] Among these structures, 19,623 were successfully ordered using the pymatgen material science analysis software.^[17]

To prioritize compounds with high probability of thermodynamic stability and high thermoelectric performance, we devised a low-fidelity performance metric as follows:

$$score_i = PF_i^{1e20,1000K} \cdot 10^{-5 \cdot E_{above\ hull}} \cdot \delta_{gap}$$

where $score_i$ is the i -type score ($i \in \{n, p\}$ -type), PF is the absolute i -type BoltzTraP^[18] maximum computed power factor at 1000 K and 10^{20} carriers cm^{-3} , $E_{above\ hull}$ is the DFT-computed energy above the convex hull (with respect to compounds in the Materials Project),^[19] and δ_{gap} is a factor for whether the material is semiconducting in an undoped state ($\delta_{gap} = 1$ if $E_{gap} = 0$, $\delta_{gap} = 0$ otherwise). To account for both possible n - and p -type doping, the maximum score was taken among both types and normalized by the number of sites (n_{sites}) in the structure:

$$score_{final} = \begin{cases} \frac{score_p}{\sqrt{n_{sites}}}, & score_p > score_n \\ \frac{score_n}{\sqrt{n_{sites}}}, & score_n > score_p \end{cases}$$

where $score_{final}$ is the final score of a compound representing a low-fidelity estimate of its thermoelectric performance and tractability for high-throughput computation. Using a dataset of 48,000 DFT-BoltzTraP calculations reported by Chen et al.,^[20] we trained a Gradient Boosting Trees ML model to predict $score_{final}$ from global symmetry features and stoichiometrically-weighted composition features generated with the data mining software matminer.^[21] The final model produced predictions on a 25% random validation set with 49% less $score_{final}$ RMSE than a dummy predictor selecting the mean $score_{final}$ of the validation set. To further validate our model, we compared the rate of selecting candidate structures in the top 1% $score_{final}$ percentile

in a “blind search” fashion on the same validation set; we found the model could identify 95% of these high-scoring candidates in less than 1/5 the calculations of a random search. The 19,623 disordered structures were then rank-ordered according to their predicted $score_{final}$.

The top 3,927 candidate structures were then computed using plane-wave DFT using PAW pseudopotentials and the Perdew-Burke-Erznherhof (PBE)^[9] functional as implemented in VASP. All DFT computations were performed using atomate,^[22] a high-throughput DFT framework. For purposes of prioritizing candidates for more in-depth computational study (as described in 2.1) the BoltzTraP^[18] package was used to predict thermoelectric power factors using a constant relaxation time of 10^{-14} s. From the most promising sets of 20 candidates for both n and p -types, the $REZnCuP_2$ compounds discussed in the main text were identified and selected for further analysis.

3. Comparison of Experimental and Computed Properties

3.1. Hole mobility

Examining the temperature dependence of the mobility provides insights into the scattering mechanisms that limit the relaxation time (**Figure S7**). When the experimental hole mobilities are fitted for $PrCuZnP_2$, the temperature dependence is found to be $T^{-1.55}$, indicating that the most likely limiting mechanism is purely acoustic phonon scattering (in theory, $\mu \propto T^{-3/2}$ for non-degenerate carriers and $\mu \propto T^{-1}$ for degenerate carriers). The temperature dependence changes from $T^{-1.33}$ for $NdCuZnP_2$ to $T^{-1.23}$ for $ErCuZnP_2$, suggesting that multiple mechanisms are at play, such as acoustic phonon scattering for degenerate and non-degenerate carriers, polar optical phonon scattering, or ionized impurity scattering. The computed hole mobilities are similar for all three compounds, with nearly identical temperature dependence of $T^{-0.74}$ indicating that polar optical phonon scattering, and, to a lesser extent, ionized impurity scattering are the limiting

mechanisms. At high temperatures, the computed mobilities become overestimated compared to the experimental values. Although grain boundary and disorder scattering can attenuate the temperature dependence (flattening the mobility curves), both mechanisms will also significantly lower the overall mobility. Because ErCuZnP_2 shows the highest experimental mobility but the weakest temperature dependence, these mechanisms cannot completely explain the discrepancy between experimental and computed values. This discrepancy may suggest we are potentially missing a scattering mode in AMSET, which could correspond to optical deformation potential scattering.

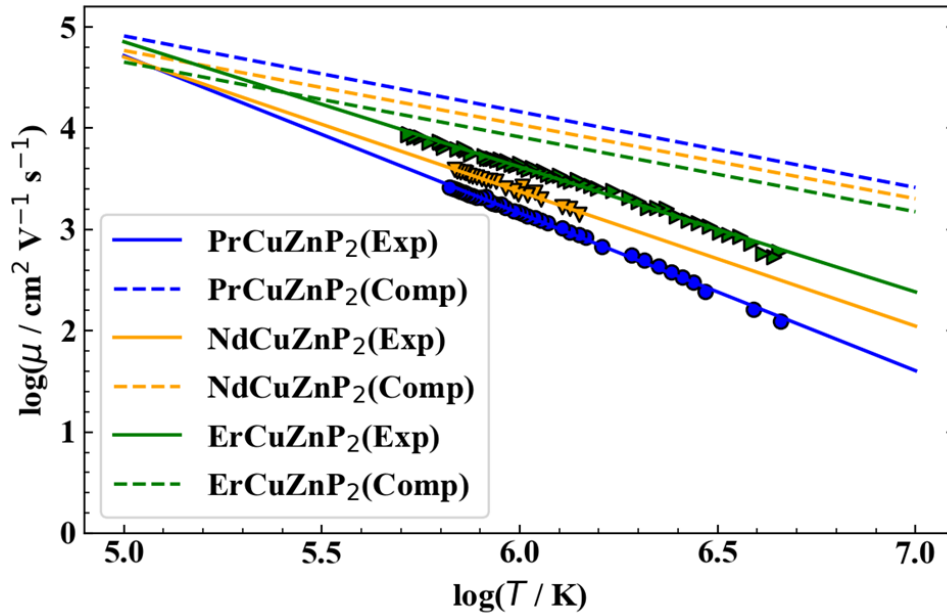


Figure S7. Temperature dependence of hole mobility. Although the computed mobilities show nearly the same temperature dependence ($T^{-0.74}$), the experimental mobilities follow flatter curves on progressing from PrCuZnP_2 ($T^{-1.55}$) to ErCuZnP_2 ($T^{-1.23}$).

3.2. Single Parabolic Band Model with Different Scattering Mechanisms

The single parabolic (SPB) model is often applied to compare mobilities and Seebeck coefficients as a function of carrier concentration (Pisarenko plot) and to guide the optimization of thermoelectric figures of merit. It is also used to extract the DOS effective mass (m_{DOS}^*) and

effective Lorenz number from experimental data, so that the electronic and phononic contributions to the thermal conductivity can be separated.

In the SPB model, electron transport is restricted to a single parabolic band subject to various scattering mechanisms. Conventionally, the electronic conduction is assumed to be limited by acoustic phonon scattering, as signaled by the temperature dependence of the mobility. However, recent thermoelectrics studies have shown that other scattering mechanisms can give rise to a similar temperature dependence. For example, even though the mobility in polycrystalline SnSe varies as $T^{-3/2}$,^[23] the dominant mechanism has been proposed to be polar optical phonon scattering instead of acoustic phonon scattering,^[24] and may be applicable to other thermoelectric materials.^[25,26,27] Until recently, first-principles electron-phonon calculations to determine scattering mechanisms have been prohibitively costly. The present results, which were obtained more manageably through AMSET, indicate that polar optical scattering dominates in $RECuZnP_2$ (**Figure 2** in main text). To examine how the type of scattering affects the transport properties calculated using the SPB model, three scattering mechanisms were considered: acoustic deformation potential (ADP), polar optical phonon (POP), and ionized impurity scattering (IMP). The relaxation times depend on energy according to:

$$\tau_{ADP}(E) = \tau_0 E^{-1/2} \quad (4)$$

$$\tau_{POP}(E) = \tau_0 \frac{E^{1/2}}{\sinh^{-1}(\sqrt{E})} \quad (5)$$

$$\tau_{IMP}(E) = \tau_0 \frac{E^{3/2}}{\ln(1+b) - \frac{b}{1+b}} \quad (6)$$

where τ_0 is the intrinsic relaxation time and $b = \frac{8m_{DOS}^* E \epsilon k_B T}{\hbar^2 n_H e^2}$ (ϵ is the dielectric constant set to the computed values (**Table S1**), k_B is the Boltzmann constant, T is the absolute temperature, \hbar is

the reduced Planck's constant, n_H is the Hall carrier concentration, and e is the elementary charge).^[28] The relaxation time for ionized impurity scattering makes use of the Brooks-Herring formula. Instead of applying the scattering parameter λ , as is commonly done in the SPB model,^[29] the relaxation times in Equations 4–6 are closer to theory, improving the accuracy of computed thermoelectric properties.^[28] The reduced chemical potential η is obtained from the experimental Seebeck coefficient:^[29]

$$S(\eta) = \frac{k_B}{e} \cdot \frac{\int_0^\infty \epsilon^{\frac{3}{2}} (\epsilon - \eta) \tau \left(-\frac{\partial f}{\partial \epsilon} \right) d\epsilon}{\int_0^\infty \epsilon^{\frac{3}{2}} \tau \left(-\frac{\partial f}{\partial \epsilon} \right) d\epsilon} \quad (7)$$

where ϵ is the reduced energy and f is the Fermi-Dirac distribution, and from there, other transport properties are calculated, as described below.

3.3. Effective Mass, Mobility, and Seebeck Coefficient

The DOS effective mass m_{DOS}^* was calculated from the reduced chemical potential, temperature, and experimental Hall carrier concentration according to:^[29]

$$n_H(\eta, T, m_{DOS}^*) = \frac{8\pi(2m_{DOS}^*k_B T)^{3/2}}{3h^3} \frac{\left(\int_0^\infty \epsilon^{\frac{3}{2}} \tau \left(-\frac{\partial f}{\partial \epsilon} \right) d\epsilon \right)^2}{\int_0^\infty \epsilon^{\frac{3}{2}} \tau^2 \left(-\frac{\partial f}{\partial \epsilon} \right) d\epsilon} \quad (8)$$

Plots of m_{DOS}^* for $RECuZnP_2$ show that it is independent of the RE cation, but strongly dependent on the scattering mechanism (**Figure S8**). The value of m_{DOS}^* remains relatively low at all temperatures for ionized impurity scattering, increases from 0.52 to 0.76 m_e as the temperature increases from 373 to 673 K for polar optical phonon scattering, and rises above 1 at 673 K for acoustic phonon scattering (**Table S3**).

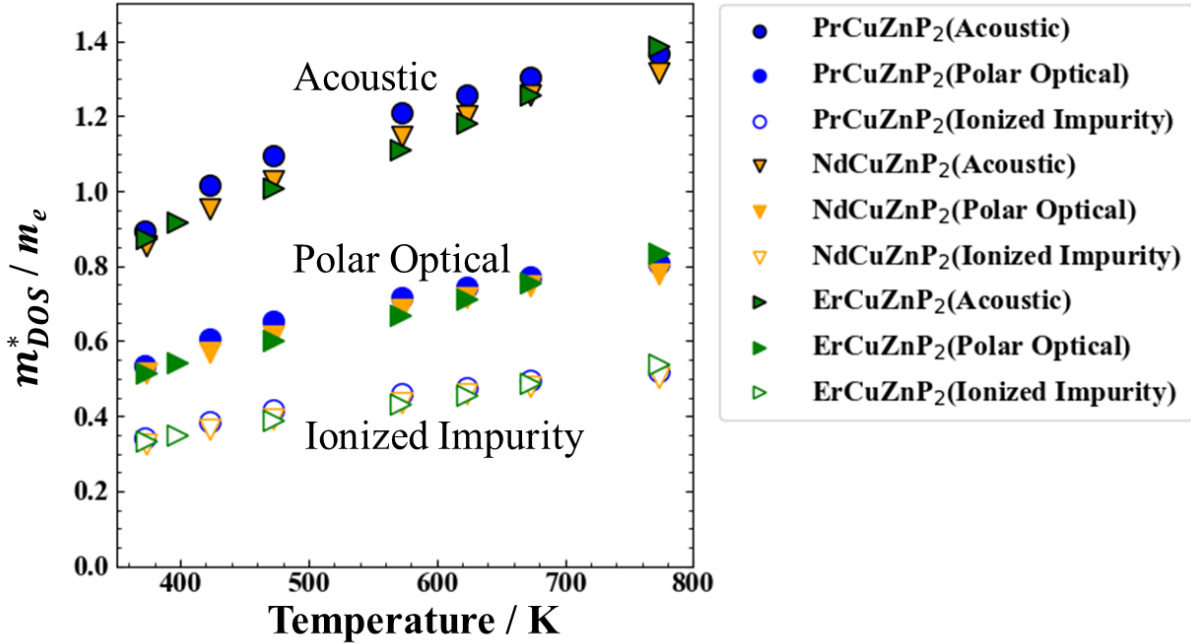


Figure S8. Temperature-dependent effective mass from density of states (m_{DOS}^*) for PrCuZnP₂, NdCuZnP₂, and ErCuZnP₂ using the single parabolic band (SPB) model with different scattering mechanisms. The increase in m_{DOS}^* with higher temperature suggests that more bands contribute to the Seebeck coefficient at higher temperature.

The electronic band structures reveal that several bands contribute to hole transport, namely a set of doubly-degenerate bands located at the valence band maximum and another band located just a few meV below (Figure S4). At 673 K, the DOS effective mass can be calculated from the degeneracy ($N_v = 3$) and the DFT predicted conductivity effective mass ($m^* = 0.37 - 0.44 m_e$) to be $m_{DOS}^* = N_v^{2/3} \cdot m^* = 0.77 - 0.90 m_e$. Similarly, at 373 K, from the degeneracy ($N_v = 2$) and the conductivity effective mass ($m^* = 0.37 - 0.43 m_e$), the DOS effective mass is $m_{DOS}^* = 0.59 - 0.68 m_e$. The SPB values agree well with the AMSET computed values for PrCuZnP₂ and NdCuZnP₂, but are overestimated for ErCuZnP₂ (Table S3), probably because the SPB model incorrectly assumes that only a single parabolic band is involved in charge transport.

Table S3. The SPB derived DOS effective mass, m_{DOS}^* , evaluated assuming acoustic phonon (ADP), polar optical phonon (POP), and ionized impurity (IMP) scattering at 373 and 673 K.

Compound	m_{DOS}^* / m_e (373 K)	m_{DOS}^* / m_e (673 K)
PrCuZnP ₂ (SPB)	0.89 (ADP); 0.54 (POP); 0.34 (IMP)	1.30 (ADP); 0.77 (POP); 0.50 (IMP)
PrCuZnP ₂ (AMSET)	0.59	0.77
NdCuZnP ₂ (SPB)	0.85 (ADP); 0.51 (POP); 0.33 (IMP)	1.26 (ADP), 0.74 (POP); 0.48 (IMP)
NdCuZnP ₂ (AMSET)	0.61	0.80
ErCuZnP ₂ (SPB)	0.88 (ADP); 0.52 (POP); 0.33 (IMP)	1.26 (ADP); 0.76 (POP); 0.49 (IMP)
ErCuZnP ₂ (AMSET)	0.68	0.90
CaZn ₂ P ₂ (AMSET)	0.98	1.00

All three *RE*CuZnP₂ compounds have lower conductivity effective mass than CaZn₂P₂ ($m^* = 0.47 - 0.48 m_e$ between 300 K to 673 K using a carrier concentration of 10^{19} cm^{-3}), because the valence bands at Γ are split less and the third band contributes to the conductivity and effective mass above 300 K. Therefore, the *RE*CuZnP₂ compounds also have lower DOS effective mass than CaZn₂P₂,^[30] consistent with their lower experimental Seebeck coefficients (**Figure 1 (d)** in the main text, **Figure S9**).

The intrinsic mobility, $\mu_0 = \tau_0 \frac{e}{m_{DOS}^*}$, is calculated from:^[29]

$$\mu_H(\eta, T, m_{DOS}^*) = \frac{e}{m_{DOS}^*} \frac{\int_0^\infty \epsilon^{\frac{3}{2}} \tau^2 \left(-\frac{\partial f}{\partial \epsilon} \right) d\epsilon}{\int_0^\infty \epsilon^{\frac{3}{2}} \tau \left(-\frac{\partial f}{\partial \epsilon} \right) d\epsilon} \quad (9)$$

using the chemical potential and the experimental Hall mobility. If the temperature and effective mass are fixed, the Hall mobility and Seebeck coefficient can be computed as a function of Hall carrier concentration using **Equations 7, 8, and 9**. The Hall mobility changes drastically with scattering mechanism and *RE* component (**Figure S10 (a)**). For acoustic phonon scattering, the mobility decreases with higher carrier concentration. For polar optical phonon scattering, the mobility barely varies with carrier concentration, and ErCuZnP₂ has the highest intrinsic mobility. The intrinsic mobility is significantly higher for ErCuZnP₂ than for PrCuZnP₂ and NdCuZnP₂, consistent with the larger grain sizes as noted earlier from the peak widths in the powder XRD patterns (**Figure S2**). For ionized impurity scattering, the mobility increases rapidly with higher carrier concentration, and ErCuZnP₂ has the lowest intrinsic mobility; these trends are in disagreement with experimental results. As implemented here, ionized impurity scattering assumes that the carrier concentration varies without change in impurity concentration. The Pisarenko plots reveal that the Seebeck coefficient is independent of scattering mechanisms and *RE* component (**Figure S10 (b)**).

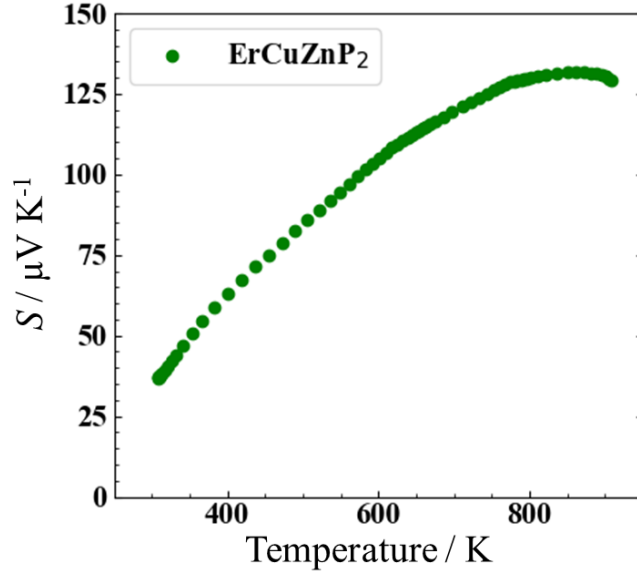


Figure S9: The Seebeck coefficient of ErCuZnP_2 whose reduction past 860 K indicates the onset of bipolar contribution.

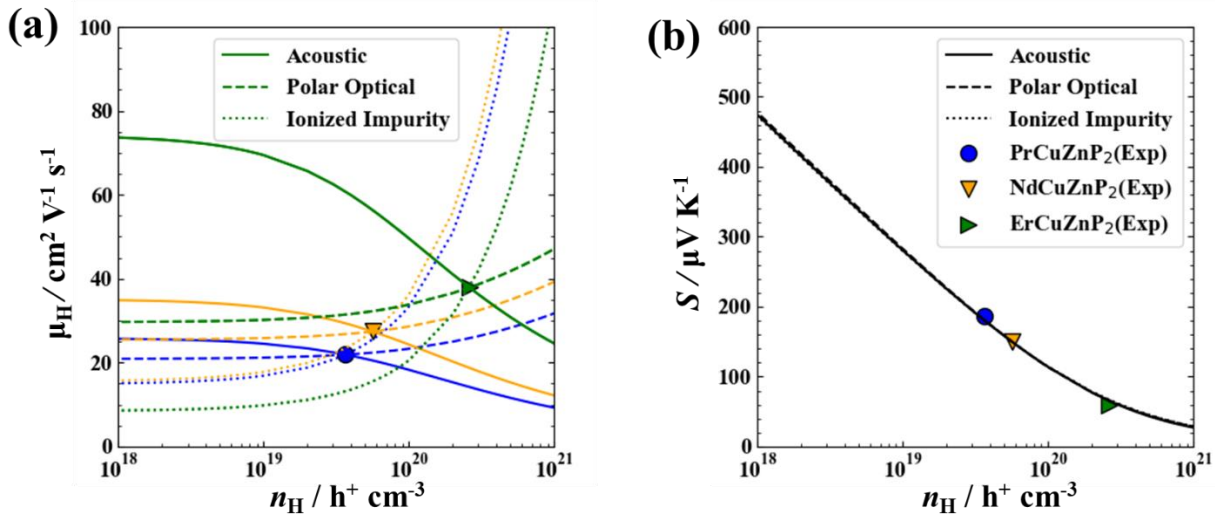


Figure S10. (a) Hall mobility and (b) Seebeck coefficient for PrCuZnP_2 (blue), NdCuZnP_2 (orange), and ErCuZnP_2 (green) as a function of Hall carrier concentration at 373 K. The extrapolations are made with the SPB model assuming acoustic phonon (solid line), polar optical phonon (dashed line), and ionized impurity scattering (dotted line) scattering mechanisms. The Hall mobility increases with heavier *RE* component (except for ionized impurity scattering), and the Seebeck coefficient is independent of *RE* component.

3.4. Electronic and Phononic Contributions to Thermal Conductivity

The total thermal conductivity consists of electronic and phononic contributions. The phononic contribution κ_{ph} is revealed by subtracting the electronic contribution κ_{el} from the total thermal conductivity. The electronic contribution can be obtained from the Wiedemann-Franz law, $\kappa_{\text{el}} = L_{\text{eff}}(T/\rho)$, which requires the effective Lorenz number L_{eff} to be determined first.

In the most common method, the Lorenz model developed by Kim et al. relates L_{eff} to experimental data, but this model assumes that scattering is limited by acoustic phonons only.^[31] Instead, the SPB model was applied to compare how different scattering mechanisms influence the effective Lorenz number, which is defined as:^[29]

$$L_{\text{eff}} = \frac{k_{\text{B}}^2 \int_0^{\infty} \epsilon^{\frac{3}{2}} \tau \left(-\frac{\partial f}{\partial \epsilon} \right) d\epsilon \int_0^{\infty} \epsilon^{\frac{3}{2}} \tau \epsilon^2 \left(-\frac{\partial f}{\partial \epsilon} \right) d\epsilon - \left(\int_0^{\infty} \epsilon^{\frac{3}{2}} \tau \epsilon \left(-\frac{\partial f}{\partial \epsilon} \right) d\epsilon \right)^2}{\left(\int_0^{\infty} \epsilon^{\frac{3}{2}} \tau \left(-\frac{\partial f}{\partial \epsilon} \right) d\epsilon \right)^2} \quad (10)$$

The effective Lorenz numbers were computed based on acoustic phonon, polar optical phonon, or ionized impurity scattering in the framework of the SPB model (left panels of **Figure S11**). These can be compared with the AMSET-computed L_{eff} values, which increase on proceeding from acoustic phonon to ionized impurity scattering. The best agreement between experimental (SPB model) and AMSET-computed L_{eff} values was found for polar optical scattering, which is consistent with the arguments presented in the main text (**Figure 2**).

Combining the SPB-calculated values of L_{eff} with the measured resistivities allows the experimental electronic contribution κ_{el} to the thermal conductivity to be determined. For all three RECuZnP_2 compounds, the AMSET-computed κ_{el} values are overestimated compared to the experimental values (middle panels of **Figure S11**), mainly because the computed electrical resistivities are underestimated (**Figure 1 (a)** in main text).

Finally, the phononic contributions κ_{ph} can be examined (right panels of **Figure S11**). For ErCuZnP_2 , the minimum phononic contribution changes from $0.72 \text{ W m}^{-1} \text{ K}^{-1}$ using ionized impurity scattering to $1.25 \text{ W m}^{-1} \text{ K}^{-1}$ using acoustic phonon scattering. The effect is less pronounced for PrCuZnP_2 ($\kappa_{\text{ph}} = 1.08$ to $1.24 \text{ W m}^{-1} \text{ K}^{-1}$) and NdCuZnP_2 ($\kappa_{\text{ph}} = 0.96 - 1.08 \text{ W m}^{-1} \text{ K}^{-1}$) because of their higher resistivities (**Figure 1 (a)** in main text). If polar optical scattering is accepted to be the operative mechanism, as shown earlier in the analysis of electron transport, then the minimum κ_{ph} values are found to be very low, varying from $1.08 \text{ W m}^{-1} \text{ K}^{-1}$ for PrCuZnP_2 to $0.96 \text{ W m}^{-1} \text{ K}^{-1}$ for ErCuZnP_2 . In fact, they approach the glassy limits for thermal conductivity determined using the experimental speeds of sound.

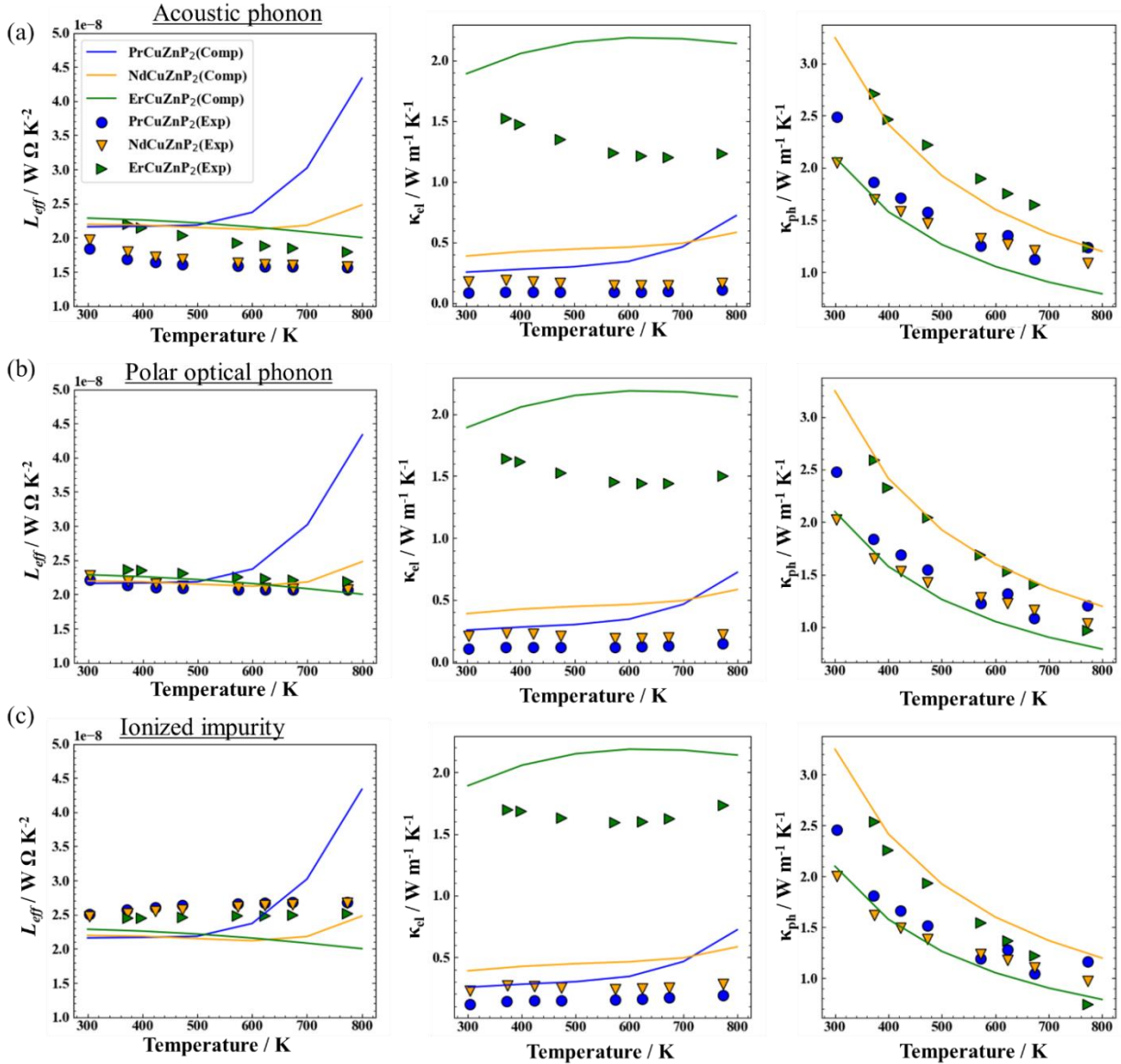


Figure S11. Effective Lorenz numbers, and electronic and phononic contributions to thermal conductivity of $RECuZnP_2$. The markers define the experiment derived SPB values (Exp) while the solid lines define the computed ASMET or CSLD results (Comp). The Lorenz number was computed using the SPB model with different scattering mechanisms: (a) acoustic phonon, (b) polar optical phonon, and (c) ionized impurity scattering. The computed Lorenz number and electronic contribution were calculated using AMSET and the phononic contribution was calculated using CSLD.

3.5. Optimization of Thermoelectric Performance

To gain insight on how to improve the thermoelectric figure of merit, which depends strongly on carrier concentration, the SPB model was applied, under the assumption that intrinsic mobility and m_{DOS}^* do not change with carrier concentration. The thermoelectric figure of merit was computed as a function of Hall carrier concentration according to:^[29]

$$zT = \frac{S^2}{L + (\beta\psi)^{-1}} \quad (11)$$

with the two parameters β and ψ defined as:

$$\beta = \frac{\mu_0 (m_{DOS}^*/m_e)^{3/2} T^{5/2}}{\kappa_{ph}} \quad (12)$$

$$\psi(\eta) = \frac{8\pi e}{3} \left(\frac{2m_e k_B}{h^2} \right)^{3/2} \int_0^\infty \epsilon^{3/2} \tau \left(-\frac{\partial f}{\partial \epsilon} \right) d\epsilon \quad (13)$$

The thermoelectric figure of merit computed using the SPB model varies with scattering mechanism (**Figure S12**). The optimum carrier concentration increases on proceeding from acoustic phonon, to polar optical phonon, to ionized impurity scattering. This trend is consistent with the differences in mobility, presented above. The computed figures of merit are higher than the experimental values because the mobilities are overestimated. As a possible way to improve the agreement, grain boundary scattering can be considered in computation of electronic and thermal transport.

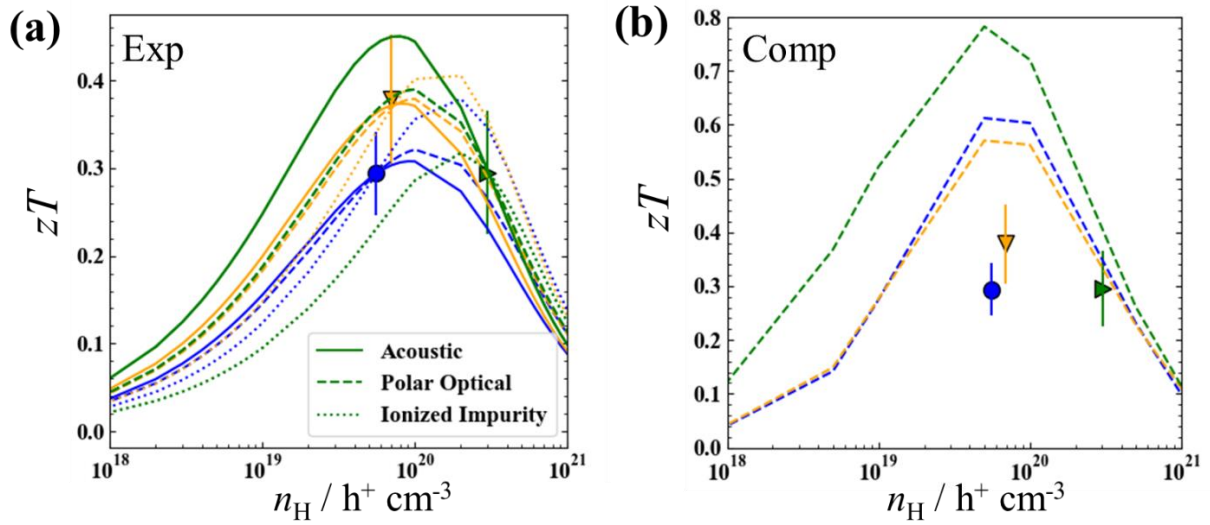


Figure S12. (a) zT as a function of carrier concentration determined using the single-parabolic band (SPB) model for PrCuZnP₂ (●), NdCuZnP₂ (▼), and ErCuZnP₂ (►) at 673 K. (b) The AMSET/CSLD computed zT values as a function of carrier concentrations overestimate the thermoelectric performance. In particular, a large difference is observed for PrCuZnP₂ and NdCuZnP₂, most likely because the scattering time is overestimated (e.g., through neglect of grain boundary scattering).

3.6. Grain Boundary Scattering

When the lattice thermal conductivity determined experimentally (using SPB and assuming polar optical phonon scattering) and computationally (using CSLD) for NdCuZnP₂ are compared, the limiting grain size appears to be 25 nm (Figure S13). Given that PrCuZnP₂ exhibits similar diffraction peak widths (Figure S2) and experimental thermal conductivities (Figure 3 in main text) as NdCuZnP₂, a grain size of 25 nm was assumed for both compounds. When the electronic and thermal properties are computed with grain boundary scattering included (Figure S14), the Seebeck coefficients decrease slightly, but the mobilities are drastically reduced, resulting in higher resistivity. However, the computed mobilities are still larger relative to experimental values, probably because the defect concentrations are underestimated or other types of scattering mechanisms (such as disorder and optical deformation potential scattering)

have been neglected. The computed total thermal conductivities agree well with experimental results when grain boundary scattering was included, and the thermoelectric figures of merit are mostly unaffected.

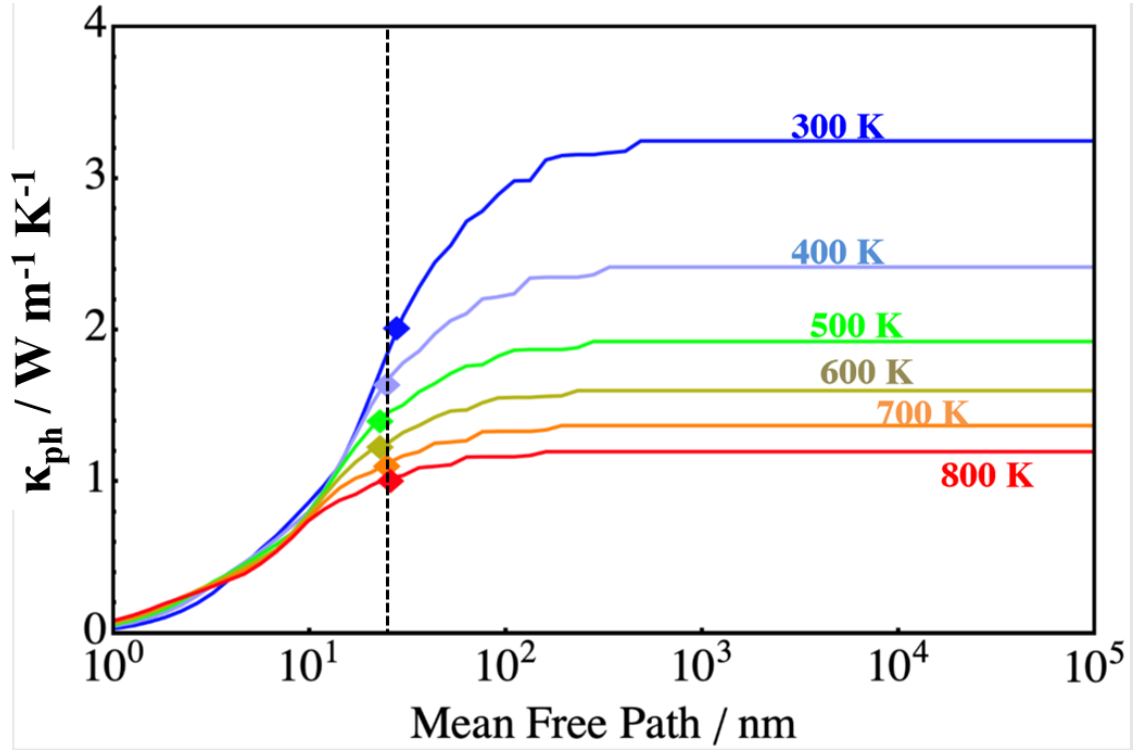


Figure S13. Phononic contribution to the thermal conductivity in NdCuZnP₂ as a function of the mean free path. Experimentally determined values are marked. The phononic thermal conductivity appears to be limited by a grain size of 25 ± 5 nm.

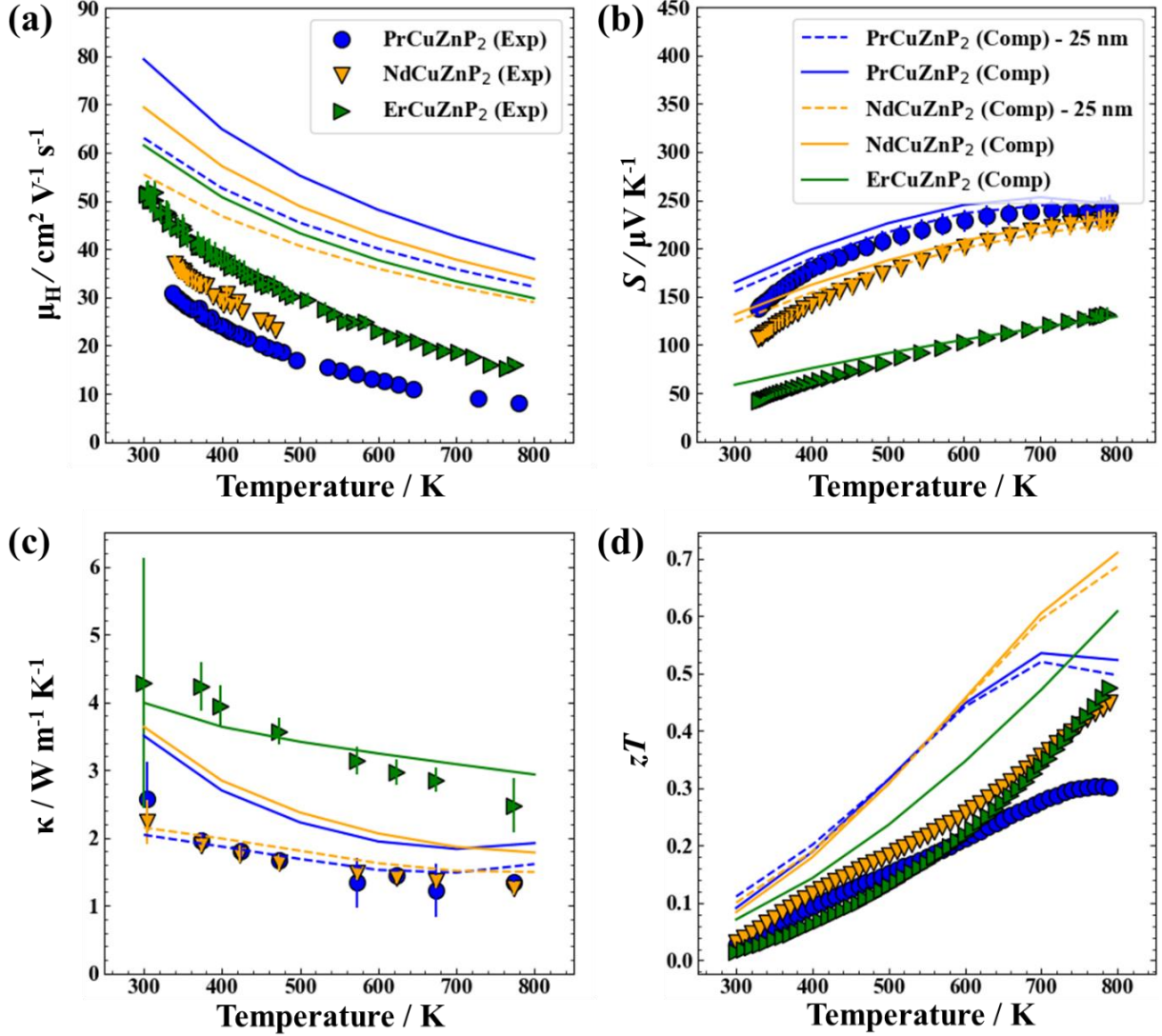


Figure S14. Experimental (markers) and computational (lines) results of (a) mobility, (b) Seebeck coefficient, (c) total thermal conductivity, and (d) figure of merit for $RECuZnP_2$. Grain boundary scattering (dashed line), assuming a grain size of 25 nm, was included for $PrCuZnP_2$ and $NdCuZnP_2$. The lattice thermal conductivity for $PrCuZnP_2$ was set to be the same as for $NdCuZnP_2$.

3.7. Mass-Disorder Scattering

Disorder scattering of phonons comes from mass disorder and strained lattice. The effect of mass disorder is given by:

$$\tau^{-1} = \frac{\pi\omega^2}{2} \sum_s \sum_a f_a(s) \left(1 - \frac{M_a}{M_s}\right)^2 |u_\lambda^*(a) \cdot u_\lambda(a)| \delta(\omega_\lambda - \omega_{\lambda'}) \quad (10)$$

with $f_a(s)$ is the fraction of atom a on site s , M_a is the mass of atom a , \widehat{M}_s is the average mass on site s , and $u_\lambda(a)$ is the eigenvector of mode λ and atom a .^[13] The strength of the scattering is determined fundamentally by the deviation of atomic masses (Cu or Zn) from their average mass. However, because Cu and Zn have minimal difference in mass, mass disorder scattering would be negligibly small (**Figure S15**). Local lattice strain due to disorder may lead to some additional lowering of lattice thermal conductivity, but the radii of Cu¹⁺ and Zn²⁺ are also nearly identical, so this is also expected to be a minor effect.

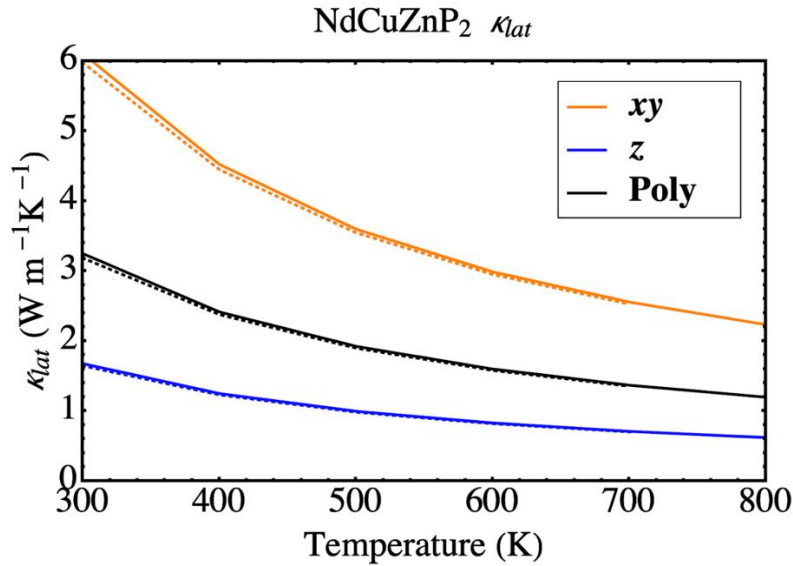


Figure S15: Computed lattice thermal conductivity with (dotted line) and without (solid line) the inclusion of mass-disordering scattering of NdCuZnP₂ using CLSD. Due to the small mass difference of Cu and Zn, mass-disordering scattering barely affects the lattice thermal conductivity.

References

- [1] P. E. R. Blanchard, S. S. Stoyko, R. G. Cavell, and A. Mar, *J. Solid State Chem.* **184**, 97 (2011).
- [2] E. S. Toberer, A. F. May, B. C. Melot, E. Flage-Larsen, G. J. Snyder, *Dalton Trans.* **2010**, 39, 1046.
- [3] H. Zhang, L. Fang, M.-B. Tang, H.-H. Chen, X.-X. Yang, X. Guo, J.-T. Zhao, Y. Grin, *Intermetallics* **2010**, *18*, 193.
- [4] A. Zevalkink, W. G. Zeier, E. Cheng, J. Snyder, J.-P. Fleurial, S. Bux, *Chem. Mater.* **2014**, *26*, 5710.
- [5] F. F. Balakirev, S. M. Ennaceur, R. J. Migliori, B. Maiorov, A. Migliori, *Rev. Sci. Instrum.* **2019**, *90*, 121401.
- [6] G. Kresse, J. Furthmüller, *Phys. Rev. B* **1996**, *54*, 11169–11186.
- [7] G. Kresse, D. Joubert, *Phys. Rev. B* **1999**, *59*, 1758–1775.
- [8] F. Zhou, W. Nielson, Y. Xia, V. Ozoliņš, *Phys. Rev. Lett.* **2014**, *113*, 185501.
- [9] J. P. Perdew, K. Burke, M. Ernzerhof, *Phys. Rev. Lett.* **1996**, *77*, 3865.
- [10] J. Heyd, G. E. Scuseria, M. Ernzerhof, *J. Chem. Phys.* **2003**, *118*, 8207–8215.
- [11] R. W. Nunes, X. Gonze, *Phys. Rev. B* **2001**, *63*, 155107.
- [12] I. Souza, J. Iñiguez, D. Vanderbilt, *Phys. Rev. Lett.* **2002**, *89*, 117602.
- [13] W. Li, J. Carrete, N. A. Katcho, N. Mingo, *Comp. Phys. Commun.* **2014**, *185*, 1747–1758.
- [14] A. Faghaninia, J. W. Ager, III, C. S. Lo, *Phys. Rev. B* **2015**, *91*, 235123.
- [15] A. Ganose, J. Park, A. Faghaninia, R. Woods-Robinson, K. A. Persson, A. Jain, arXiv:2008.09734v1 [cond-mat.mtrl-sci] 22 Aug 2020.
- [16] G. Bergerhoff, I. Brown and F. Allen, Crystallographic Databases, International Union of Crystallography, Chester, 1987.
- [17] S. P. Ong, W. D. Richards, A. Jain, G. Hautier, M. Kocher, S. Cholia, D. Gunter, V. L. Chevrier, K. A. Persson, G. Ceder, *Comput. Mater. Sci.* **2013**, *68*, 314–319.
- [18] G. K. Madsen and D. J. Singh, *Comput. Phys. Commun.* **2006**, *175*, 67–71.
- [19] A. Jain, S. P. Ong, G. Hautier, W. Chen, W. D. Richards, S. Dacek, S. Cholia, D. Gunter, D. Skinner, G. Ceder, K. A. Persson, *APL Mater.* **2013**, *1*, 011002.
- [20] W. Chen, J.-H. Pöhl, G. Hautier, D. Broberg, S. Bajaj, U. Aydemir, Z. M. Gibbs, H. Zhu, M. Asta, G. J. Snyder, B. Meredig, M. A. White, K. Persson, and A. Jain, *J. Mater. Chem. C* **2016**, *4*, 4414–4426.
- [21] L. Ward, A. Dunn, A. Faghaninia, N. E. R. Zimmermann, S. Bajaj, Q. Wang, J. Montoya, J. Chen, K. Bystrom, M. Dylla, K. Chard, M. Asta, K. A. Persson, G. J. Snyder, I. Foster, and A. Jain, *Comput. Mater. Sci.* **2018**, *152*, 60–69.
- [22] K. Mathew, J. H. Montoya, A. Faghaninia, S. Dwarakanath, M. Aykol, H. Tang, I.-h. Chu, T. Smidt, B. Bocklund, M. Horton, J. Dagdelen, B. Wood, Z.-K. Liu, J. Neaton, S. P. Ong, K. Persson, and A. Jain, *Comput. Mater. Sci.* **2017**, *139*, 140–152.
- [23] C.-L. Chen, H. Wang, Y.-Y. Chen, T. Day, G. J. Snyder, *J. Mater. Chem. A* **2014**, *2*, 11171.
- [24] J. Ma, Y. Chen, W. Li, *Phys. Rev. B* **2018**, *97*, 205207.
- [25] J. Cao, J. D. Querales-Flores, A. R. Murphy, S. Fahy, I. Savić, *Phys. Rev. B* **2018**, *98*, 205202.
- [26] J. Zhou, H. Zhu, T.-H. Liu, Q. Song, R. He, J. Mao, Z. Liu, W. Ren, B. Liao, D. J. Singh, Z. Ren, G. Chen, *Nat. Commun.* **2018**, *9*, 1721.
- [27] J. Park, Y. Xia, and V. Ozoliņš, *Phys. Rev. Appl.* **2019**, *11*, 014058.
- [28] M. Lundstrom, *Fundamentals of carrier transport*, 2nd Edition, Cambridge University Press, Cambridge, UK **2008**.
- [29] A. F. May, E. S. Toberer, A. Saramat, G. J. Snyder, *Phys. Rev. B: Condens. Matter Mater. Phys.* **2009**, *80*, 125205.
- [30] V. Ponnambalam, S. Lindsey, W. Xie, D. Thompson, F. Drymiotis, T. M. Tritt, *J. Phys. D: Appl. Phys.* **2011**, *44*, 155406.
- [31] H.-S. Kim, Z. M. Gibbs, Y. Tang, H. Wang, G. J. Snyder, *APL Mater.* **2015**, *3*, 041506.